

# HATs: Hierarchical Adaptive Taxonomy Segmentation for Panoramic Pathology Image Analysis

Ruining Deng<sup>1</sup>, Quan Liu<sup>1</sup>, Can Cui<sup>1</sup>, Tianyuan Yao<sup>1</sup>, Juming Xiong<sup>1</sup>, Shunxing Bao<sup>1</sup>, Hao Li<sup>1</sup>, Mengmeng Yin<sup>2</sup>, Yu Wang<sup>2</sup>, Shilin Zhao<sup>2</sup>, Yucheng Tang<sup>3</sup>, Haichun Yang<sup>2</sup>, and Yuankai Huo<sup>1,2</sup>

1. Vanderbilt University, Nashville TN 37215, USA,
2. Vanderbilt University Medical Center, Nashville TN 37232, USA,
3. NVIDIA Corporation, Santa Clara and Bethesda, USA

**Abstract.** Panoramic image segmentation in computational pathology presents a remarkable challenge due to the morphologically complex and variably scaled anatomy. For instance, the intricate organization in kidney pathology spans multiple layers, from regions like the cortex and medulla to functional units such as glomeruli, tubules, and vessels, down to various cell types. In this paper, we propose a novel Hierarchical Adaptive Taxonomy Segmentation (HATs) method, which is designed to thoroughly segment panoramic views of kidney structures by leveraging detailed anatomical insights. Our approach entails (1) the innovative HATs technique which translates spatial relationships among 15 distinct object classes into a versatile “plug-and-play” loss function that spans across regions, functional units, and cells, (2) the incorporation of anatomical hierarchies and scale considerations into a unified simple matrix representation for all panoramic entities, (3) the adoption of the latest AI foundation model (EfficientSAM) as a feature extraction tool to boost the model’s adaptability, yet eliminating the need for manual prompt generation in conventional segment anything model (SAM). Experimental findings demonstrate that the HATs method offers an efficient and effective strategy for integrating clinical insights and imaging precedents into a unified segmentation model across more than 15 categories. The official implementation is publicly available at <https://github.com/hrlblab/HATs>.

## 1 Introduction

In renal pathology, accurate diagnosis [31], severity assessment [25], and treatment efficacy [24] rely on detailed examination across multiple structural levels, from broad regions (like medulla and cortex) to specific functional units (glomerulus, tubules, vessels, etc.) and individual cells. The detailed quantification across multiple organs has led to the widespread exploration of pathomics [3, 7, 8, 17, 22] as a fully quantitative approach, enhancing the current semi-quantitative clinical guidance and enabling the development of fully quantitative biomarkers. While numerous studies have advanced the segmentation of pathological images for detailed tissue analysis using deep learning techniques [5, 14, 27, 32, 37], they face primary challenges: current architectures, which often incorporate multiple networks or heads [12, 20, 23, 28, 34, 38], typically target individual tissue types or those within similar size ranges. These approaches lack a holistic

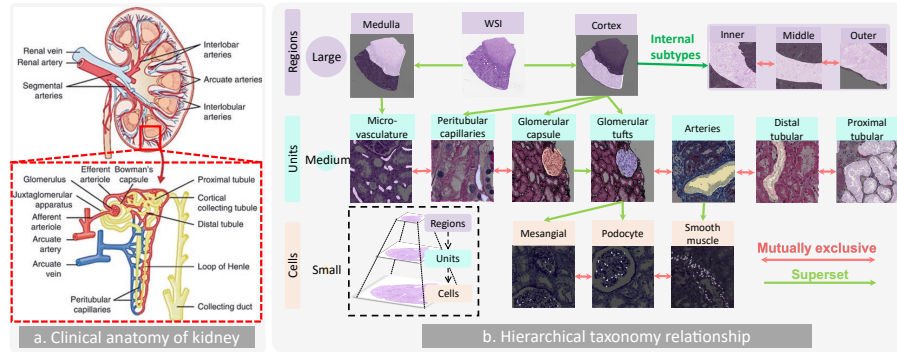


**Fig. 1. Knowledge transformation from kidney anatomy to a hierarchical taxonomy tree.**

This figure demonstrates the transformation of intricate clinical anatomical relationships within the kidney into a hierarchical taxonomy tree. (a) Pathologists examine histopathology in accordance with kidney anatomy. (b) This study revisits kidney anatomy using a hierarchical semantic taxonomy for panoramic segmentation, covering 15 classes across regions, units, and cells. The tree incorporates spatial relationships into a semi-supervised learning paradigm and uses hierarchical scale information as prior knowledge to weigh the relationship between classes.

strategy for segmentation across various anatomical levels, from broad regions to specific cells. The intricate spatial dynamics among these entities, depicted in Fig. 1, are crucial for comprehensive segmentation success. However, this holistic view has not been fully integrated into current deep learning advancements, leaving the complete segmentation of kidney anatomy [1] unattained.

Recently, the Segment Anything Model (SAM) [26] has been proposed to provide comprehensive segmentation for everything. Many studies have endeavored to incorporate this foundational model into digital pathology [9, 10, 30]. However, there lacks a fine-tuning paradigm specifically aimed at resolving semantic segmentation challenges without explicit pixel-level prompts within foundational model architectures.

In this work, we propose a novel Hierarchical Adaptive Taxonomy Segmentation (HATs) method, which is designed to thoroughly segment panoramic views of kidney structures by leveraging detailed anatomical insights. A hierarchical adaptive taxonomy matrix and a hierarchical scale matrix are established to translate anatomical relationships into computational modeling concepts. Moreover, The proposed method leverages the state-of-the-art AI foundation models [9, 10, 26, 30] and a token-based EfficientSAM [36]. It integrates class and scale knowledge into a dynamic token bank, employing weak token prompts instead of pixel-wise ones for efficient segmentation. The contribution of this paper is threefold:

- The HATs method is proposed for mathematically modeling clinical anatomy with a hierarchical taxonomy matrix and a hierarchical scale matrix for panoramic pathology segmentation. It models hierarchical spatial relationships of 15 object classes, across regions, functional units, and cells;

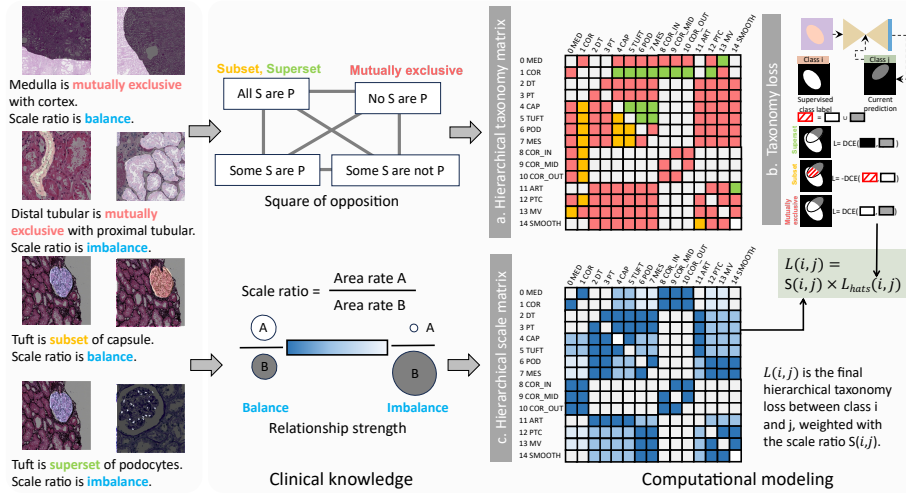


**Fig. 2. hierarchical taxonomy learning** – This figure highlights the key innovation of the proposed taxonomy learning strategy. (a) A hierarchical taxonomy matrix is modeled from anatomical relationships to Aristotle’s logic theory in pathological image segmentation. (b) A novel taxonomy loss function is designed to operationalize the affirmative and negatory relationships from hierarchical taxonomy matrix during the training process. (c) We further encode a hierarchical scale matrix to illustrate the strength of the relationship between different objects in kidney anatomy.

- A token-based dynamic EfficientSAM [36] network architecture that leverages weak token prompts to replace pixel-wise prompts to achieve superior semantic segmentation of images with partial labels, while storing class-aware knowledge and scale-aware knowledge with a token bank.

- The holistic design of hierarchical matrix representation, token bank, and AI foundation model allows a single dynamic model to achieve comprehensive pathology image analysis.

## 2 Methods

The panoramic pathology segmentation comprises three integral components: (1) a hierarchical taxonomy matrix with a taxonomy loss (Fig. 2), (2) a hierarchical scale matrix to weight the strength of relationships in hierarchical taxonomy loss (Fig. 2), and (3) a dynamic EfficientSAM network with a token bank.

### 2.1 Hierarchical taxonomy matrix with taxonomy loss

This anatomical relationship is characterized by the hierarchical taxonomy tree, as shown in Fig. 1b, through: **Uniqueness**. Each pair of objects is connected by a single proposition on the hierarchical tree. The expanding structure of the map, devoid

of cycles, ensures stable inheritance relationships from regions down to cellular levels. **Transmissibility.** Indirect relationships between objects can be inferred from direct relationships, as established by the two fundamental categorical propositions. Relationships between objects not directly connected can be determined by combining propositions along their connecting paths on the tree. Inspired by previous work [13], we introduce an expanded 15-class hierarchical taxonomy matrix (as depicted in Fig. 2a),  $M_t \in \mathbb{R}^{n \times n}$ , to facilitate implementation in computational models. Here,  $n$  represents the number of classes within the map. The matrix values includes subset ( $\subseteq$ ), superset ( $\supseteq$ ), and mutually exclusive ( $\cap = \emptyset$ ).

With the introduction of the hierarchical taxonomy matrix, we incorporate spatial correlation into the training process for comprehensive segmentation using a novel taxonomy loss (as depicted in Fig. 2b). For a given image  $I$  with a labeled class  $i$ , represented as  $Y_i$ , we generate predictions  $Y'_j$  for another class  $j$  within the same image. We then use the anatomical relationship to supervise the correlation between the supervised label  $Y_i$  and the semi-supervised prediction  $Y'_j$ : (1) If  $i$  is a superset of  $j$ , then  $Y'_j$  should not exceed the region of  $Y_i$ ; conversely, (2) if  $i$  is a subset of  $j$ , then  $Y'_j$  should cover  $Y_i$  as comprehensively as possible; and (3) if  $i$  and  $j$  are mutually exclusive, the overlap between  $Y_i$  and  $Y'_j$  should be minimized. The total taxonomy loss is defined by the following equations:

$$L_{\text{hats}}(i, j) = \begin{cases} \text{DCE}(1 - Y_i, Y'_j), & \text{if } i \subseteq j \\ -\text{DCE}(Y_i, Y_i \cup Y'_j), & \text{if } i \supseteq j \\ \text{DCE}(Y_i, Y'_j), & \text{if } i \cap j = \emptyset \\ 0, & \text{if otherwise} \end{cases} \quad (1)$$

where DCE denotes the Dice Loss.

## 2.2 Hierarchical scale matrix with area ratio knowledge

We formed pairwise spatial relationships across all 15 objects in the hierarchical taxonomy matrix. However, in the hierarchical taxonomy tree, different objects have varying levels of supervisory power over anatomical knowledge, depending on the size of the object and the scale of the images. For example, it is challenging to recognize explicit cells in region images at  $5\times$  magnification, while global regional knowledge is less useful and informative in cell images at  $20\times$  magnification. Therefore, we further incorporate hierarchical scale knowledge into taxonomy learning, translating hierarchical taxonomy matrix from a binary relationship [13] to a fully quantitative relationship.

The hierarchical scale matrix for the 15 objects is calculated for the entire dataset to represent the strength of the relationship between two objects by their area rates, shown in Table 1. The area rate ( $a$ ) for each object is determined by multiplying the pixel mean of each object in the images by the square of the micron value, and then dividing by the size of the patches. This process provides a standardized measure of an object’s size in both digital and real-world dimensions.

With the area rate ( $a$ ) listed in Table 1, we evaluate the strength of the spatial relationship in each pair of objects as the value in the hierarchical scale matrix ( $S$ ) using the formula in Fig. 2c:

**Table 1.** Data collection and scale rate

Class	Stain	Patch #	Size (pixel <sup>2</sup> )	Scale (×)	Micron (μm/pixel)	Pixel mean (pixel <sup>2</sup> )	Area rate ((μm/pixel) <sup>2</sup> )
Medulla	P	1,619	1024 <sup>2</sup>	5	2	637,975	2.434
Cortex	P	3,055	1024 <sup>2</sup>	5	2	681,392	2.600
Inn. Cor.	P	1,242	1024 <sup>2</sup>	5	2	461,277	1.760
Mid. Cor.	P	1,357	1024 <sup>2</sup>	5	2	485,849	1.853
Out. Cor.	P	1,586	1024 <sup>2</sup>	5	2	483,486	1.844
DT	H,P,S,T	4,615	256 <sup>2</sup>	10	1	6,381	0.097
PT	H,P,S,T	4,588	256 <sup>2</sup>	10	1	23,605	0.360
Cap.	H,P,S,T	4,559	256 <sup>2</sup>	5	2	10,140	0.619
Tuft	H,P,S,T	4,536	256 <sup>2</sup>	5	2	7,641	0.466
Art.	H,P,T	4,875	256 <sup>2</sup>	10	1	5,446	0.083
PTC	P	4,827	256 <sup>2</sup>	40	0.25	2,152	0.002
MV	P	1,362	512 <sup>2</sup>	20	0.5	12,905	0.012
Pod.	P	1,147	512 <sup>2</sup>	20	0.5	1,170	0.001
Mes.	P	789	512 <sup>2</sup>	20	0.5	1,079	0.001
Smooth.	P	1,326	512 <sup>2</sup>	20	0.5	2,527	0.002

\*Inn. is inner; Mid. is middle; out. is Outer; Cor. is cortex;

\*DT is distal tubular; PT is proximal tubular; \*Cap. is glomerular capsule; Tuft is glomerular tuft;

\*Art. is arteries; MV is micro-vasculature; PTC is peritubular capillaries;

\*Pod. is podocyte cell; Mes. is mesangial cell; Smooth. is smooth muscle

\*H is H&E; P is PAS; S is SIL; T is TRI.

The total loss function is an aggregate of supervised and semi-supervised losses in 2, weighted by  $\lambda_{\text{hats}}$

$$L(i) = \text{DCE}(Y_i, Y'_i) + \text{BCE}(Y_i, Y'_i) + \lambda_{\text{hats}} \sum_{j=1}^n S(i, j) \times L_{\text{hats}}(i, j) \quad (j \neq i) \quad (2)$$

where BCE represents the Binary Cross-Entropy loss.  $Y'_i$  is the prediction for class  $i$ .

### 2.3 Dynamic EfficientSAM with token bank

The architecture of dynamic EfficientSAM is presented in Fig. 3. The backbone of our proposed network, EfficientSAM [36], is chosen for its superior segmentation performance and efficient computation. Instead of using pixel-level prompts for each object in the image, a pre-defined learnable token bank is initialized to store the class-specific and scale-specific knowledge among the whole dataset. Dimensionally stable class-aware tokens ( $T_c \in \mathbb{R}^{n \times d}$ ) and scale-aware tokens ( $T_s \in \mathbb{R}^{4 \times d}$ ) are employed from the token bank to capture the contextual information in the model. Each class has a one-dimensional token,  $t_c \in \mathbb{R}^{1 \times d}$ , to store class-specific knowledge at the feature level across the entire dataset, while each magnification scale has a one-dimensional token,  $t_s \in \mathbb{R}^{1 \times d}$ , to provide scale-specific knowledge across four scales (5×, 10×, 20×, and 40×).

There are three module parts that use these conditional tokens to achieve semantic segmentation in the network: (1) Inspired by the Vision Transformer (ViT) [15], for an image  $I$  of class  $i$  with magnification  $m$ , the corresponding class token  $T_c(i)$  and scale

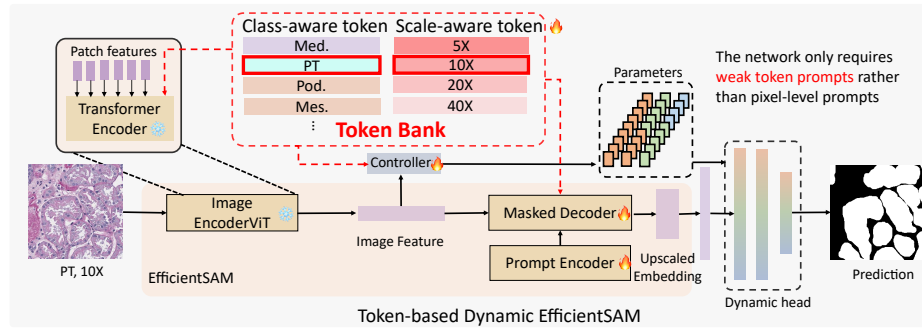


**Fig. 3. Dynamic EfficientSAM with token bank** – This figure visualizes the architecture of our proposed token-based dynamic EfficientSAM. Key components include a dynamic token bank with class-aware and scale-aware tokens, a token-guided imageViT encoder, a mask decoder, and a dynamic head network. This architecture leverages AI foundation model by fine-tuning with weak tokens, liberating the model from the need for pixel-level image prompts.

token  $T_s(m)$  are stacked with the patch-wise image tokens before being fed into the current transformer block ( $E_b$ ) (as shown in 3); (2)  $T_c(i)$  and  $T_s(m)$  are concatenated with latent image features ( $F$ ) from the imageViT encoder ( $E$ ) and a Global Average Pooling ( $GAP$ ) in  $\mathbb{R}^d$  for parameters ( $\omega$ ) in the dynamic head (as shown in 4); (3)  $T_c(i)$  and  $T_s(m)$  also serve as sparse embeddings combined with dense embedding ( $E_d$ ) in the Mask Decoder ( $M_d$ ) to produce upscaled embeddings ( $e_{upscale}$ ) (as shown in 5).

$$e_b = E_b(T_c[i] || T_s[m] || e_{b-1}) \quad (3)$$

$$\omega = \varphi(\text{GAP}(F) || T_c[i] || T_s[m]; \Theta_\varphi) \quad (4)$$

$$e_{upscale} = M_d(\text{GAP}(F) || T_c[i] || T_s[m] || E_d) \quad (5)$$

Where  $||$  represents the stacking operation,  $\Theta_\varphi$  denotes the number of parameters in the dynamic head. The final semantic segmentation logits are obtained as the output of the dynamic head, inspired by [12].

### 3 Data and Experiments

**Data.** Our model leverages a 15-class, partially labeled dataset spanning various biological scales, from regions to cells. The dataset’s structure is detailed in Table 1. We sourced the human kidney dataset from three distinct resources across regions, functional units and cells. Detailed data introduction can be found in the supplementary material. The dataset was partitioned into training, validation, and testing sets at a 6:1:3 ratio across all classes, with splits conducted at the patient level to prevent data leakage.

**Experiment Details.** The training process of our model was divided into two distinct phases. In the initial phase, which spanned the first 50 epochs, we employed a supervised learning strategy focused on minimizing binary Dice loss and cross-entropy loss. Subsequently, for the remaining epochs, both supervised and semi-supervised learning

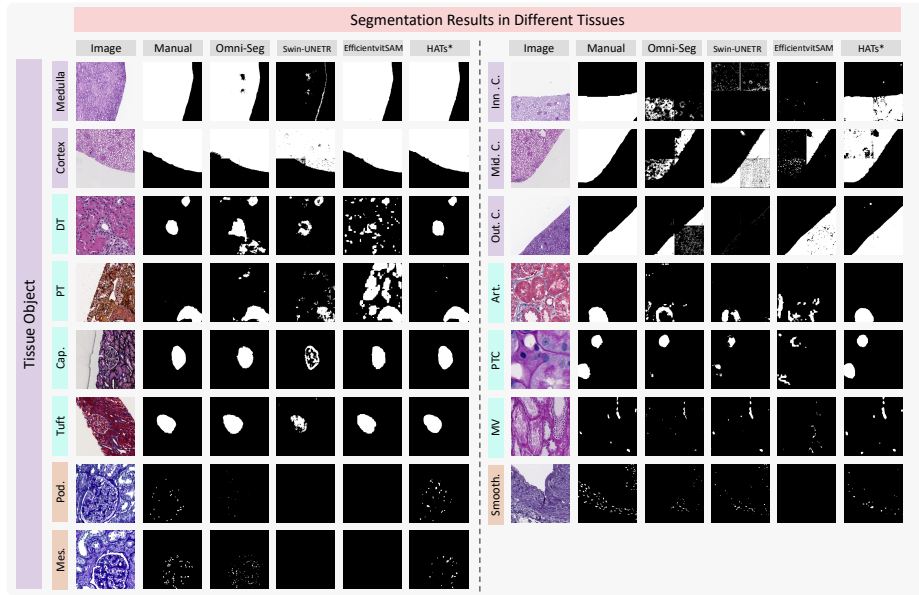


**Fig. 4. Validation qualitative results** – This figure shows the qualitative results of different approaches. The proposed method achieved superior panoramic kidney pathology segmentation on 15 classes range regions to cells with fewer false positives, false negatives, and morphological errors.

strategies were utilized, incorporating anatomy loss to explore the spatial correlation among multiple objects. All images were either randomly cropped or padded to a uniform size of  $512 \times 512$  pixels prior to being fed into the model in the training stage. Testing images were initially processed using either center-cropping or non-overlapping tiling to attain the same uniform size  $512 \times 512$  pixels. In our experiments,  $\lambda_{\text{hats}}$  was set to 0.1. All experiments were conducted on a uniform platform, specifically a workstation equipped with an NVIDIA RTX A6000 GPU.

## 4 Results

We conducted a comparative analysis of our proposed hierarchical taxonomy learning with the dynamic EfficientSAM approach against various baseline models. These models include multi-class segmentation architectures such as (1) U-Nets [16], (2) DeepLabV3 [29], (3) Residual-U-Net [33], (4) a CNN-based multi-class kidney pathology model [6], (5) Omni-Seg [12], (6) a CNN-based panoramic segmentation PrPSeg [13], (7) SegFormer [35], (8) UNETR [19], (9) Swin-UNETR [18], and (10) Efficient-ViT-SAM [39].

Table 2 and Fig. 4 demonstrates that our proposed method, HATs, surpasses baseline models in most evaluated metrics. Fig. 4 further highlights the qualitative superiority of our approach, evidenced by reduced instances of false positives, false negatives,



and morphological errors. The Dice similarity coefficient (Dice: %, the higher, the better) was employed as the primary metric for quantitative performance assessment. The results indicate that, while multi-head designs struggle with managing spatial relationships between objects (e.g., subset/superset relationships between the capsule and tuft), the dynamic-head paradigm exhibits superior performance compared to other methods. The proposed method achieves better average performance across 15 categories.

**Table 2.** Performance on panoramic segmentation for kidney pathology. Dice similarity coefficient scores (%) are reported. The difference between the reference (Ref.) method and benchmarks is statistically evaluated by Wilcoxon signed-rank test. All abbreviations are defined in Table 1

Method	Backbone	Regions				Functional units					Cells			Average	Statistic.			
		Med.	Cor.	Inn.	C. Out.	C. DT	PT	Cap.	Tufts	Art.	PTC	MV	Pod.			Mes.	Smooth.	
U-Nets [16]	CNN	23.87	64.03	34.53	32.36	33.62	47.61	60.45	45.36	46.62	47.32	49.21	48.66	49.92	49.87	49.77	45.55	$p < 0.001$
DeepLabV3 [29]	CNN	27.31	62.10	34.53	33.13	33.67	53.88	62.19	76.88	74.54	58.32	62.52	48.93	49.92	49.87	49.77	51.84	$p < 0.001$
Residual-U-Net [33]	CNN	24.29	62.24	34.53	30.53	47.77	65.76	78.12	69.62	79.64	54.74	60.72	57.29	66.20	49.87	56.77	55.87	$p < 0.001$
Multi-kidney [6]	CNN	22.81	68.37	34.54	30.35	33.60	67.90	67.70	85.21	54.87	55.04	55.66	68.35	<b>66.65</b>	49.87	64.28	55.02	$p < 0.001$
Omni-Seg [12]	CNN	64.91	70.56	40.16	36.32	58.07	63.73	77.44	87.87	88.00	56.11	65.22	55.76	60.30	62.64	60.93	63.20	$p < 0.001$
PrPSeg [13]	CNN	65.21	70.16	39.52	36.92	69.72	66.61	78.70	89.85	89.97	60.79	65.90	64.79	64.57	<b>62.98</b>	63.44	65.94	$p < 0.001$
SegFormer [35]	Transformer	21.90	65.84	34.53	31.51	34.01	58.56	72.01	66.87	55.57	52.50	62.76	48.69	58.47	54.44	52.34	51.33	$p < 0.001$
UNETR [19]	Transformer	23.72	69.43	34.52	29.57	33.71	57.54	71.67	72.14	51.62	51.36	54.74	55.86	49.92	49.87	49.96	50.37	$p < 0.001$
Swin-UNETR [18]	Transformer	24.13	69.75	34.33	29.97	33.83	<b>68.05</b>	75.40	78.51	72.59	<b>65.91</b>	63.74	68.54	49.95	49.87	<b>66.54</b>	56.74	$p < 0.001$
Efficientvit-SAM [39]	SAM	63.17	71.29	38.77	<b>48.69</b>	70.63	57.20	68.96	89.73	91.04	49.48	59.13	48.87	49.92	49.87	49.80	60.44	$p < 0.001$
HATs (Ours)	SAM	<b>67.69</b>	<b>72.83</b>	<b>49.66</b>	47.86	<b>71.61</b>	64.03	<b>79.30</b>	<b>91.97</b>	<b>93.02</b>	62.19	<b>68.30</b>	<b>68.55</b>	59.53	60.01	57.06	<b>67.58</b>	<b>Ref.</b>

**Table 3.** Ablation study of different design. Dice similarity coefficient scores (%) are reported. The difference between the reference (Ref.) method and benchmarks is statistically evaluated by Wilcoxon signed-rank test. \*HTM is Hierarchical Taxonomy Matrix with taxonomy loss, HSM is Hierarchical Scale Matrix

Backbone	HTM	HSM	Regions	Units	Cells	Average	Statistic.
Omni-Seg [12]			53.99	70.59	61.29	63.20	$p < 0.001$
Swin-UNETR [18]			38.41	70.39	55.45	56.74	$p < 0.001$
Efficientvit-SAM [39]			58.51	66.35	49.86	60.44	$p < 0.001$
PrPSeg (CNN) [13]			54.96	73.02	62.77	64.95	$p < 0.001$
PrPSeg (CNN) [13]		✓	56.31	73.80	<b>63.64</b>	65.94	$p < 0.001$
PrPSeg (CNN) [13]		✓	56.35	75.03	63.48	66.65	$p < 0.001$
HATs (d-EfficientSAM) (Ours)			57.60	74.77	57.71	65.63	$p < 0.001$
HATs (d-EfficientSAM) (Ours)		✓	60.45	74.98	58.74	66.89	$p < 0.001$
HATs (d-EfficientSAM) (Ours)		✓	<b>61.93</b>	<b>75.34</b>	58.87	<b>67.58</b>	<b>Ref.</b>

**Ablation study.** Table 3 showcases the enhancements brought about by our proposed token-based EfficientSAM and learning strategies. The results indicate that the token-based dynamic EfficientSAM generally achieves better performance in segmenting objects at all levels. With the integration of the hierarchical taxonomy matrix and hierarchical scale matrix, performance across all considered metrics is enhanced. Additionally, the performance of the proposed matrices is also evaluated with the CNN backbone



from PrPSeg. The results demonstrate the generalizability and comprehensive enhancement of the matrices. However, there is a limitation: transformer-based methods exhibit better segmentation for large-scale objects (regions, objects, etc.), while CNN-based methods achieve superior performance on smaller objects (cells). It is promising to extend the current backbone by combining CNN and transformer architectures to enhance segmentation capabilities in the future work.

## 5 Conclusion

In this work, we introduce the Hierarchical Adaptive Taxonomy Segmentation method, an innovative approach for panoramic kidney structure segmentation that harnesses in-depth anatomical understanding. By formulating both a hierarchical adaptive taxonomy matrix and a hierarchical scale matrix, we successfully convert anatomical relationships into computational models. Utilizing advanced AI foundation models along with a token-based EfficientSAM, our method incorporates class and scale knowledge into a dynamic token bank, favoring weak token prompts over traditional pixel-wise prompts in the SAM-based model for enhanced efficiency in segmentation. The contributions of this study pave the way for comprehensive pathology image analysis with a single dynamic model.

**Acknowledgements.** This research was supported by NIH R01DK135597(Huo), DoD HT9425-23-1-0003(HCY), NIH NIDDK DK56942(ABF). This work was also supported by Vanderbilt Seed Success Grant, Vanderbilt Discovery Grant, and VISE Seed Grant. This project was supported by The Leona M. and Harry B. Helmsley Charitable Trust grant G-1903-03793 and G-2103-05128. This research was also supported by NIH grants R01EB033385, R01DK132338, REB017230, R01MH125931, and NSF 2040462. We extend gratitude to NVIDIA for their support by means of the NVIDIA hardware grant.

**Disclosure of Interests.** The authors have no competing interests.

## References

1. AL-Mamari, S.A.: Anatomy of the Kidney, pp. 3–16. Springer Nature Singapore, Singapore (2023), [https://doi.org/10.1007/978-981-99-6171-9\\_1](https://doi.org/10.1007/978-981-99-6171-9_1)
2. Bankhead, P., Loughrey, M.B., Fernández, J.A., Dombrowski, Y., McArt, D.G., Dunne, P.D., McQuaid, S., Gray, R.T., Murray, L.J., Coleman, H.G., et al.: Qupath: Open source software for digital pathology image analysis. *Scientific reports* **7**(1), 1–7 (2017)
3. Barisoni, L., Lafata, K.J., Hewitt, S.M., Madabhushi, A., Balis, U.G.: Digital pathology and computational image analysis in nephropathology. *Nature Reviews Nephrology* **16**(11), 669–685 (2020)
4. Barisoni, L., Nast, C.C., Jennette, J.C., Hodgin, J.B., Herzenberg, A.M., Lemley, K.V., Conway, C.M., Kopp, J.B., Kretzler, M., Lienczewski, C., et al.: Digital pathology evaluation in the multicenter nephrotic syndrome study network (neptune). *Clinical Journal of the American Society of Nephrology* **8**(8), 1449–1459 (2013)
5. Bel, T.d., Hermsen, M., Litjens, G., Laak, J.: Structure instance segmentation in renal tissue: a case study on tubular immune cell detection. In: *Computational Pathology and Ophthalmic Medical Image Analysis*, pp. 112–119. Springer (2018)

6. Bouteldja, N., Klinkhammer, B.M., Bülow, R.D., Droste, P., Otten, S.W., von Stillfried, S.F., Moellmann, J., Sheehan, S.M., Korstanje, R., Menzel, S., et al.: Deep learning-based segmentation and quantification in experimental kidney histopathology. *Journal of the American Society of Nephrology* **32**(1), 52–68 (2021)
7. Chen, J., Wang, Y., Deng, R., Liu, Q., Cui, C., Yao, T., Liu, Y., Zhong, J., Fogo, A.B., Yang, H., et al.: Spatial pathomics toolkit for quantitative analysis of podocyte nuclei with histology and spatial transcriptomics data in renal pathology. In: *Medical Imaging 2024: Digital and Computational Pathology*. vol. 12933, pp. 252–260. SPIE (2024)
8. Chen, R.J., Lu, M.Y., Wang, J., Williamson, D.F., Rodig, S.J., Lindeman, N.I., Mahmood, F.: Pathomic fusion: an integrated framework for fusing histopathology and genomic features for cancer diagnosis and prognosis. *IEEE Transactions on Medical Imaging* **41**(4), 757–770 (2020)
9. Cui, C., Deng, R., Liu, Q., Yao, T., Bao, S., Remedios, L.W., Tang, Y., Huo, Y.: All-in-sam: from weak annotation to pixel-wise nuclei segmentation with prompt-based finetuning. *arXiv preprint arXiv:2307.00290* (2023)
10. Deng, R., Cui, C., Liu, Q., Yao, T., Remedios, L.W., Bao, S., Landman, B.A., Wheless, L.E., Coburn, L.A., Wilson, K.T., et al.: Segment anything model (sam) for digital pathology: Assess zero-shot segmentation on whole slide imaging. *arXiv preprint arXiv:2304.04155* (2023)
11. Deng, R., Li, Y., Li, P., Wang, J., Remedios, L.W., Agzamkhodjaev, S., Asad, Z., Liu, Q., Cui, C., Wang, Y., et al.: Democratizing pathological image segmentation with lay annotators via molecular-empowered learning. In: *International Conference on Medical Image Computing and Computer-Assisted Intervention*. pp. 497–507. Springer (2023)
12. Deng, R., Liu, Q., Cui, C., Yao, T., Long, J., Asad, Z., Womick, R.M., Zhu, Z., Fogo, A.B., Zhao, S., et al.: Omni-seg: A scale-aware dynamic network for renal pathological image segmentation. *IEEE Transactions on Biomedical Engineering* (2023)
13. Deng, R., Liu, Q., Cui, C., Yao, T., Yue, J., Xiong, J., Yu, L., Wu, Y., Yin, M., Wang, Y., et al.: Prpseg: Universal proposition learning for panoramic renal pathology segmentation. In: *Proceedings of the IEEE/CVF Conference on Computer Vision and Pattern Recognition*. pp. 11736–11746 (2024)
14. Ding, H., Pan, Z., Cen, Q., Li, Y., Chen, S.: Multi-scale fully convolutional network for gland segmentation using three-class classification. *Neurocomputing* **380**, 150–161 (2020)
15. Dosovitskiy, A., Beyler, L., Kolesnikov, A., Weissenborn, D., Zhai, X., Unterthiner, T., Dehghani, M., Minderer, M., Heigold, G., Gelly, S., et al.: An image is worth 16x16 words: Transformers for image recognition at scale. *arXiv preprint arXiv:2010.11929* (2020)
16. González, G., Washko, G.R., San José Estépar, R.: Multi-structure segmentation from partially labeled datasets. application to body composition measurements on ct scans. In: *Image Analysis for Moving Organ, Breast, and Thoracic Images*, pp. 215–224. Springer (2018)
17. Gupta, R., Kurc, T., Sharma, A., Almeida, J.S., Saltz, J.: The emergence of pathomics. *Current Pathobiology Reports* **7**, 73–84 (2019)
18. Hatamizadeh, A., Nath, V., Tang, Y., Yang, D., Roth, H.R., Xu, D.: Swin unetr: Swin transformers for semantic segmentation of brain tumors in mri images. In: *International MICCAI Brainlesion Workshop*. pp. 272–284. Springer (2021)
19. Hatamizadeh, A., Tang, Y., Nath, V., Yang, D., Myronenko, A., Landman, B., Roth, H.R., Xu, D.: Unetr: Transformers for 3d medical image segmentation. In: *Proceedings of the IEEE/CVF winter conference on applications of computer vision*. pp. 574–584 (2022)
20. Hermsen, M., de Bel, T., Den Boer, M., Steenberg, E.J., Kers, J., Florquin, S., Roelofs, J.J., Stegall, M.D., Alexander, M.P., Smith, B.H., et al.: Deep learning-based histopathologic assessment of kidney tissue. *Journal of the American Society of Nephrology* **30**(10), 1968–1979 (2019)

21. Howard, A., HCL-Jevster, Gustilo, K., Borner, K., Ryan, H., Jain, Y.: Hubmap - hacking the human vasculature (2023), <https://kaggle.com/competitions/hubmap-hacking-the-human-vasculature>
22. Huo, Y., Deng, R., Liu, Q., Fogo, A.B., Yang, H.: Ai applications in renal pathology. *Kidney international* **99**(6), 1309–1320 (2021)
23. Jayapandian, C.P., Chen, Y., Janowczyk, A.R., Palmer, M.B., Cassol, C.A., Sekulic, M., Hodgkin, J.B., Zee, J., Hewitt, S.M., O’Toole, J., et al.: Development and evaluation of deep learning–based segmentation of histologic structures in the kidney cortex with multiple histologic stains. *Kidney international* **99**(1), 86–101 (2021)
24. Jiménez-Heffernan, J., Bajo, M.A., Perna, C., del Peso, G., Larrubia, J.R., Gamallo, C., Sánchez-Tomero, J., López-Cabrera, M., Selgas, R.: Mast cell quantification in normal peritoneum and during peritoneal dialysis treatment. *Archives of pathology & laboratory medicine* **130**(8), 1188–1192 (2006)
25. Kellum, J.A.: Acute kidney injury. *Critical care medicine* **36**(4), S141–S145 (2008)
26. Kirillov, A., Mintun, E., Ravi, N., Mao, H., Rolland, C., Gustafson, L., Xiao, T., Whitehead, S., Berg, A.C., Lo, W.Y., et al.: Segment anything. arXiv preprint arXiv:2304.02643 (2023)
27. Kumar, N., Verma, R., Sharma, S., Bhargava, S., Vahadane, A., Sethi, A.: A dataset and a technique for generalized nuclear segmentation for computational pathology. *IEEE transactions on medical imaging* **36**(7), 1550–1560 (2017)
28. Li, Y., Huang, X., Wang, Y., Xu, Z., Sun, Y., Zhang, Q.: U-net ensemble model for segmentation in histopathology images (2019)
29. Lutnick, B., Ginley, B., Govind, D., McGarry, S.D., LaViolette, P.S., Yacoub, R., Jain, S., Tomaszewski, J.E., Jen, K.Y., Sarder, P.: An integrated iterative annotation technique for easing neural network training in medical image analysis. *Nature machine intelligence* **1**(2), 112–119 (2019)
30. Ma, J., He, Y., Li, F., Han, L., You, C., Wang, B.: Segment anything in medical images. *Nature Communications* **15**(1), 654 (2024)
31. Mounier-Vehier, C., Lions, C., Devos, P., Jaboureck, O., Willoteaux, S., Carre, A., Beregi, J.P.: Cortical thickness: an early morphological marker of atherosclerotic renal disease. *Kidney international* **61**(2), 591–598 (2002)
32. Ren, J., Sadimin, E., Foran, D.J., Qi, X.: Computer aided analysis of prostate histopathology images to support a refined gleason grading system. In: *Medical Imaging 2017: Image Processing*. vol. 10133, p. 101331V. International Society for Optics and Photonics (2017)
33. Salvi, M., Mogetta, A., Gambella, A., Molinaro, L., Barreca, A., Papotti, M., Molinari, F.: Automated assessment of glomerulosclerosis and tubular atrophy using deep learning. *Computerized Medical Imaging and Graphics* **90**, 101930 (2021)
34. Wu, H., Pang, S., Sowmya, A.: Tgnet: A task-guided network architecture for multi-organ and tumour segmentation from partially labelled datasets. In: *2022 IEEE 19th International Symposium on Biomedical Imaging (ISBI)*. pp. 1–5. IEEE (2022)
35. Xie, E., Wang, W., Yu, Z., Anandkumar, A., Alvarez, J.M., Luo, P.: Segformer: Simple and efficient design for semantic segmentation with transformers. *Advances in Neural Information Processing Systems* **34**, 12077–12090 (2021)
36. Xiong, Y., Varadarajan, B., Wu, L., Xiang, X., Xiao, F., Zhu, C., Dai, X., Wang, D., Sun, F., Iandola, F., et al.: EfficientSAM: Leveraged masked image pretraining for efficient segment anything. arXiv preprint arXiv:2312.00863 (2023)
37. Zeng, C., Nan, Y., Xu, F., Lei, Q., Li, F., Chen, T., Liang, S., Hou, X., Lv, B., Liang, D., et al.: Identification of glomerular lesions and intrinsic glomerular cell types in kidney diseases via deep learning. *The Journal of pathology* **252**(1), 53–64 (2020)
38. Zhang, J., Xie, Y., Xia, Y., Shen, C.: Dodnet: Learning to segment multi-organ and tumors from multiple partially labeled datasets. In: *Proceedings of the IEEE/CVF Conference on Computer Vision and Pattern Recognition*. pp. 1195–1204 (2021)

39. Zhang, Z., Cai, H., Han, S.: Efficientvit-sam: Accelerated segment anything model without performance loss. arXiv preprint arXiv:2402.05008 (2024)

# HATs: Hierarchical Adaptive Taxonomy Segmentation for Panoramic Pathology Image Analysis

Supplementary Materials

## 1 Data Introduction

Our model leverages a 15-class, partially labeled dataset spanning various biological scales, from regions to cells. We sourced the human kidney dataset from three distinct resources:

### 1.1 Regions

Whole slide images of wedge kidney sections stained with periodic acid-Schiff (PAS,  $n=138$ ) were obtained from non-cancerous regions of nephrectomy samples. The samples were categorized into several groups based on clinical data, including normal adults ( $n=27$ ), patients with hypertension (HTN,  $n=31$ ), patients with diabetes (DM,  $n=4$ ), patients with both hypertension and diabetes ( $n=14$ ), normal aging individuals ( $\text{age} > 65\text{y}$ ,  $n=10$ ), individuals with aging and hypertension ( $n=36$ ), and individuals with aging, hypertension, and diabetes ( $n=16$ ). These tissues were scanned at  $20\times$  magnification and manually annotated in QuPath [2], delineating medulla, inner cortex, middle cortex, and outer cortex contours. The WSIs were downsampled to  $5\times$  magnification and segmented into  $1024\times 1024$  pixel patches. Corresponding binary masks were derived from the contours.

### 1.2 Functional Units

**NEPTUNE** The distal tubular, proximal tubular, glomerular capsule, glomerular tufts, arteries, and peritubular capillaries are from the NEPTUNE study [4] with 459 WSIs, encompassing 125 patients with minimal change disease, we extracted 1,751 Regions of Interest (ROIs). These ROIs were manually segmented to identify four kinds of morphology objects with normal structure and methodology outlined in [23]. Each image, at a resolution of  $3000\times 3000$  pixels ( $40\times$  magnification,  $0.25\ \mu\text{m}$  per pixel), represented one of four tissue types stained with Hematoxylin and Eosin Stain (H&E), PAS, Silver Stain (SIL), and Trichrome Stain (TRI). We treated these four staining methods as color augmentations and resized the images to  $256\times 256$  pixels, maintaining the original data splits from [23].

**HuBMAP** Complementing the NEPTUNE dataset, we also incorporated data from HuBMAP. This dataset is comprised of 5 PAS-stained WSIs from varied donors, chosen based on criteria such as image quality (minimal artifacts or blurring), demographic diversity (considering age, sex, BMI), and encompassing different kidney regions (cortical, medullary, papillary). Expert segmentation was performed on the WSIs using

QuPath by a lead anatomist, assisted by four other trained anatomists. They identified three types of microvascular structures: arterial/arteriole, peritubular capillary/vasa recta, vein/venule. These were later grouped under a single category termed “microvasculature” [21]. The WSIs were then transformed into patches of dimensions  $512 \times 512$  at a  $20 \times$  magnification.

### 1.3 Cells

We employed 17 WSIs of normal adult cases from the aforementioned nephrectomy dataset. These pathology images were scanned at  $20 \times$  magnification and cropped into  $512 \times 512$  pixel segments to facilitate cell labeling, following the annotation process described in [11].